Geophysical Journal International

Geophys. J. Int. (2019) **219,** 1334–1347
Advance Access publication 2019 August 12
GJI Seismology

doi: 10.1093/gji/ggz370

Post-critical *SsPmp* and its applications to Virtual Deep Seismic Sounding (VDSS) – 2: 1-D imaging of the crust/mantle and joint constraints with receiver functions

Tianze Liu [1], Simon L. Klemperer,[1] Gabriel Ferragut[1,2,*] and Chunquan Yu[3,†]

[1] *Department of Geophysics, Stanford University, Stanford, CA 94305, USA. E-mail: tianze@stanford.edu*
[2] *Department of Geosciences, North Dakota State University, Fargo, ND 58105, USA*
[3] *Seismological Laboratory, California Institute of Technology, Pasadena, CA 91125, USA*

Accepted 2019 August 9. Received 2019 August 2; in original form 2019 February 19

SUMMARY

Virtual Deep Seismic Sounding (VDSS) has emerged as a novel method to image the crust–mantle boundary (CMB) and potentially other lithospheric boundaries. In Part 1, we showed that the arrival time and waveform of post-critical *SsPmp*, the post-critical reflection phase at the CMB used in VDSS, is sensitive to several different attributes of the crust and upper mantle. Here, we synthesize our methodology of deriving Moho depth, average crustal V_p and uppermost-mantle V_p from single-station observations of post-critical *SsPmp* under a 1-D assumption. We first verify our method with synthetics and then substantiate it with a case study using the Yellowknife and POLARIS arrays in the Slave Craton, Canada. We show good agreement of crustal and upper-mantle properties derived with VDSS with those given by previous active-source experiments and our own *P* receiver functions (PRF) in our study area. Finally, we propose a PRF-VDSS joint analysis method to constrain average crustal V_p/V_s ratio and composition. Our PRF-VDSS joint analysis shows that the southwest Slave Craton has an intermediate crustal composition, most consistent with a Mesoarchean age.

Key words: Body waves; Composition and structure of the continental crust; Cratons; Crustal imaging; North America; Wave scattering and diffraction.

1 INTRODUCTION

In recent years, Virtual Deep Seismic Sounding (VDSS) has been used to measure Moho depth in different areas (e.g. Tseng *et al*. 2009; Yu *et al*. 2012, 2016; Tian *et al*. 2015; Kang *et al*. 2016; Parker *et al*. 2016; Thompson *et al*. 2019). *SsPmp*, the seismic phase used in VDSS, originates when upcoming teleseismic *S* waves convert to downgoing *P* waves at the free surface (the virtual source), which then undergo post-critical reflection at or within the crust–mantle boundary (CMB) and finally reach the receiver (Fig. 1). (Here we use CMB to denote the boundary or geological transition from crust to mantle, whether abrupt or a 'velocity-gradient zone' spanning many kilometres; and *Moho* to denote a seismological inference about this transition, typically given as a single depth.) The arrival time of *SsPmp* relative to the direct *S* arrival (or *Ss*), hereafter T_{VDSS}, is used to estimate the Moho depth at the reflection point, commonly assumed to be the midpoint between the virtual source and receiver. Because VDSS uses teleseismic events, the incident *S* wave is usually approximated as a plane wave with constant ray parameter. To enable post-critical reflection of *SsPmp* at the CMB, appropriate epicentral distances are ∼30–50° (Yu *et al*. 2016), corresponding to ray parameter $p = \sim$0.1256–0.1409 s km^{-1} for a focal depth of 0 km ($1/p = \sim$7.10–7.96 km s^{-1}), and slightly smaller p for larger focal depths (Fig. 2 in Liu *et al*., 2018, hereafter Part 1). Due to post-critical reflection at the CMB, *SsPmp* usually has amplitude comparable to *Ss* (Aki & Richards 2002a, Fig. 1b), making it possible to construct a seismic profile with a single event recorded by an array. Because *SsPmp* undergoes post-critical reflection at the CMB, its phase is changed relative to *Ss* (Fig. 1b; hereafter referred to as phase shift for simplicity and denoted Φ_{VDSS}), making it difficult to directly pick T_{VDSS} from raw records. Previous studies (e.g. Tseng *et al*. 2009; Tian *et al*. 2015; Yu *et al*. 2016) used 1-D waveform fitting to measure T_{VDSS} and then found the trade-off relation between average crustal V_p (V_p^{av}) and thickness H using the equation:

$$T_{VDSS} = 2H\sqrt{\frac{1}{V_p^{av\,2}} - p^2}, \tag{1}$$

where p is the ray parameter of *Ss* and *SsPmp*. In Part 1, we used 1-D synthetic tests to show that whereas T_{VDSS} is primarily determined

* Now at: Department of Earth Sciences, University of Oregon, Eugene, OR 97403, USA
† Now at: Department of Earth and Space Sciences, Southern University of Science and Technology, Guangdong Sheng 518055, China

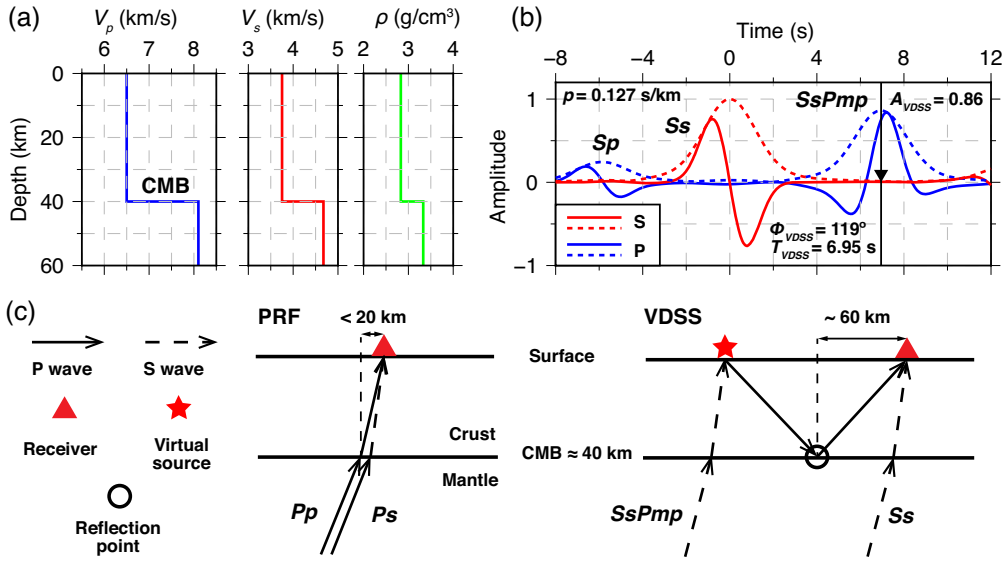

Figure 1. (a) 1-D V_p, V_s and density model ('Model #1'). (b) *P*- and *S*-component synthetic seismograms ('observed waveforms') computed with Model #1 for a ray parameter $p = 0.127$ s km^{-1} (epicentral distance of ~48.5°). The dashed curves are corresponding envelope functions. Here and throughout this paper, *P* components are blue and *S* components red. Note the high amplitude and large phase shift of *SsPmp* relative to *Ss*. (c) Comparison between ray paths of P receiver functions (PRF) and Virtual Deep Seismic Sounding (VDSS).

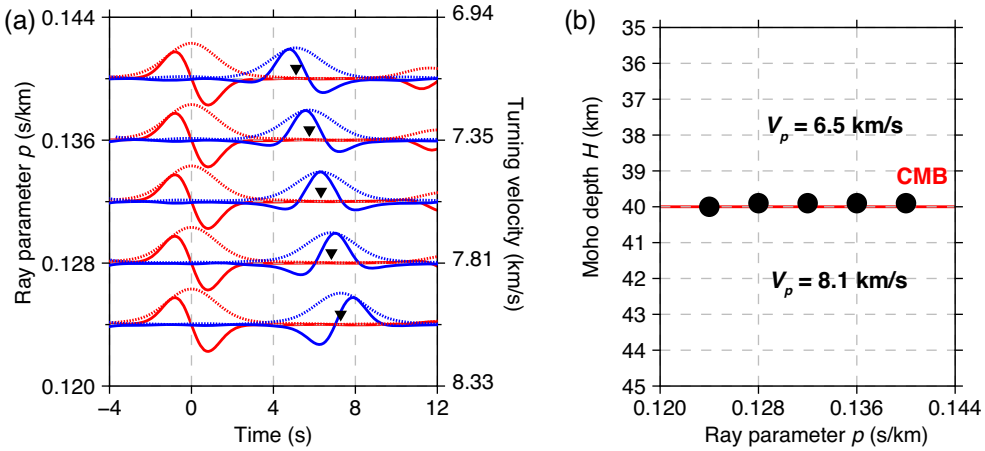

Figure 2. (a) Solid curves: *P*- (blue) and *S*-component (red) synthetic waveforms ('observed waveforms') computed with Model #1 for ray parameter $p = 0.124$–0.140 s km^{-1}. Dotted curves: envelope functions. Black triangles: theoretical T_{VDSS} computed for Model #1, always located at the peak of the *P*-component envelope functions despite the change in Φ_{VDSS}. (b) Black circles: Moho depths derived from T_{VDSS} estimated by picking peaks on *P* envelope functions and converting to depth using the correct average crustal $V_p = 6.5$ km s^{-1}. Red line: true CMB depth at 40 km.

by CMB depth and V_p^{av}, Φ_{VDSS} is sensitive to lower-crustal and uppermost-mantle V_p (V_p^{lc} and V_p^{um}), which implies the possibility of constraining both V_p^{lc} and V_p^{um} with observations of Φ_{VDSS}.

Here, we first show that we can estimate T_{VDSS} by picking peaks on *SsPmp* envelope functions and use it to derive Moho depth (Parker *et al*. 2016). We then present synthetic tests to demonstrate that V_p^{um} can be constrained without a priori knowledge of V_p^{lc} using post-critical *SsPmp* with turning velocity $1/p$ close to V_p^{um}. In the presence of noise, we show that the estimation of V_p^{um} can be significantly improved by incorporating Φ_{VDSS} measurements from multiple events. In addition, we propose a joint PRF-VDSS analysis scheme that simultaneously constrains V_p^{av} and average crustal V_p/V_s ratio, thus crustal average composition (V_p/V_s ratio is also denoted κ, particularly when used in context of the H–κ analysis of receiver functions: Zhu & Kanamori 2000). Finally, we validate our proposed methods using the Yellowknife and POLARIS arrays in the SW Slave Craton, finding good agreement between the crustal and upper-mantle properties we derive with VDSS and those from previous studies using active-source experiments and our own *P* receiver functions (PRF). We demonstrate with our PRF-VDSS joint analysis that the SW Slave Craton has an intermediate crustal composition.

2 SYNTHETIC EXAMPLES

2.1 Measuring T_{VDSS} from envelope functions

When a signal undergoes a phase shift, its envelope function stays constant despite the changing waveform, (Aki & Richards 2002a). Therefore, a simple way to account for the phase shift of *SsPmp*

relative to *Ss* while measuring T_{VDSS} is to calculate the time between the peaks on *Ss* and *SsPmp* envelope functions (Parker *et al*. 2016). Fig. 2(a) shows synthetic waveforms calculated using the reflectivity algorithm (Randall 1989) for the 1-D models in Fig. 1 (hereafter 'Model #1') and $0.124 \leq p \leq 0.140$ s km^{-1}, after separation into pseudo-*P* (motion associated with incoming *P* waves) and pseudo-*S* (motion associated with incoming *S* waves) components (hereafter referred to as *P* and *S* for simplicity) with a particle-motion analysis algorithm (Yu *et al*. 2013) and converting to envelope functions. The shapes of *Ss* (*S* component) and *SsPmp* (*P* component) envelope functions are essentially identical, as the arrivals are only distinguished by a phase shift (Φ_{VDSS}), a negligible amplitude change due to post-critical reflection, and a time delay. We then measure T_{VDSS} from these *Ss* and *SsPmp* envelope functions and convert them to Moho depths using eq. (1) and the true V_p^{av}. The estimated Moho depths agree (within 0.1 km) with the true CMB depth for all p (Fig. 2b), indicating the robustness of this method. Given multiple *SsPmp* observations with a wide range of ray parameter p, one can simultaneously determine Moho depth and V_p^{av} (Kang *et al*. 2016), as shown below. Although T_{VDSS} can be robustly estimated from *SsPmp* envelope functions, when calculating these envelope functions we effectively eliminate the information contained in Φ_{VDSS} (Fig. 2a), which is sensitive to the structure of the CMB (Part 1). Therefore, a more desirable way to analyse *SsPmp* is to model T_{VDSS} and Φ_{VDSS} simultaneously.

2.2 Modeling T_{VDSS} and Φ_{VDSS} simultaneously for a single event

In order to model T_{VDSS} and Φ_{VDSS} simultaneously, we first generate synthetic *SsPmp* waveforms for all combinations of V_p in the lower crust (V_p^{lc}) and upper mantle (V_p^{um}) using the reflection coefficient at the Moho (Aki & Richards 2002b). We then use cross-correlation to align the synthetic *SsPmp* waveforms with the 'observed' data (e.g. the waveforms in Fig. 1b) and compute the normalized misfit (hereafter referred to as misfit for simplicity) between the synthetic and 'observed' *SsPmp*. Before computing the misfit, we normalize the 'observed' and synthetic *SsPmp* by the peak values of their envelope functions so that the effects of amplitude difference are eliminated. The synthetic *SsPmp* waveform with the minimum misfit determines the best-fitting V_p^{lc} and V_p^{um}, and the best-fitting T_{VDSS} is found by picking the peak cross-correlation value between the best-fitting synthetic *SsPmp* and the 'observed' one. We note that previous 1-D modelling schemes have held V_p^{lc} and/or V_p^{um} fixed (Tseng *et al*. 2009; Tian *et al*. 2015; Yu *et al*. 2016). To test our approach, we use the reflectivity method (Randall 1989) to compute 'observed' waveforms and try to recover T_{VDSS}, V_p^{lc} and V_p^{um} from them using the method described above.

We first attempt to recover both V_p^{lc} and V_p^{um} from the observed *SsPmp* waveforms. Our 'observed' waveforms are computed with Model #1, a single layer crust with $V_p = 6.5$ km s^{-1} overlaying a half space with $V_p = 8.1$ km s^{-1} that represents the upper mantle (Fig. 1a). We use two different ray parameters $p = 0.128$ and 0.136 s km^{-1} to study the potential effects of ray parameter. After applying our proposed method, the resulting misfits are plotted as functions of V_p^{lc} and V_p^{um} (Fig. 3). In the case with $p = 0.128$ s km^{-1} ($1/p = 7.81$ km s^{-1}), we observe that the misfit depends strongly on V_p^{um} and weakly on V_p^{lc}, with the misfit contours having small negative slopes (negative trade-off between V_p^{lc} and V_p^{um}; Fig. 3a). In contrast, in the case with $p = 0.136$ s km^{-1} ($1/p = 7.35$ km s^{-1}), although the trade-off between V_p^{lc} and V_p^{um} is still negative, the misfit depends weakly on both V_p^{lc} and V_p^{um} (Fig. 3b). [Note that because the observed and synthetic waveforms are not computed in the same way, minor differences exist between them that makes the minimum misfits in both cases non-zero (Fig. 3).] Because fitting *SsPmp* waveforms is equivalent to fitting Φ_{VDSS}, this behaviour of misfit can be understood by considering the dependence of Φ_{VDSS} on V_p^{lc} and V_p^{um}. When $1/p$ is close to V_p^{um}, for example the case with $p = 0.128$ s km^{-1} ($1/p = 7.81$ km s^{-1}; Fig 3a), Φ_{VDSS} is primarily controlled by V_p^{um} with only weak dependence on V_p^{lc} (Fig. 7a in Part 1). When $1/p$ is close to neither V_p^{um} nor V_p^{lc}, for example the case with $p = 0.136$ s km^{-1} ($1/p = 7.35$ km s^{-1}; Fig. 3b), Φ_{VDSS} depends weakly on both V_p^{um} and V_p^{lc} (Part 1). Ideally, when $1/p$ is close to V_p^{lc}, misfit will be primarily controlled by V_p^{lc} due to the strong dependence of Φ_{VDSS} on V_p^{lc} (Fig. 7b in Part 1). However, in this case the large p may cause strong pre-critical reflections from intracrustal interfaces that may interfere with *SsPmp* and distort its waveform (e.g. Fig. 5 in Part 1). Therefore, a more practical way to utilize Φ_{VDSS} observations is to infer V_p^{um} from Φ_{VDSS} while assuming a known V_p^{lc} in cases with $1/p$ close to V_p^{um}, because in such cases an incorrect V_p^{lc} would only have limited effect on estimated V_p^{um} (Fig. 3a).

Fig. 4 shows examples of this strategy of estimating Moho depth and V_p^{um} from *SsPmp* waveforms while fixing V_p^{lc}. We use the correct $V_p^{av} = 6.5$ km s^{-1} in eq. (1) to convert the measured T_{VDSS} to Moho depth. For $p = 0.128$ s km^{-1}, when the true $V_p^{lc} = 6.5$ km s^{-1} (V_p^{lc} and V_p^{av} are the same here because the crust is homogeneous) is assumed, we are able to recover both the CMB depth and V_p^{um} precisely (Fig. 4a). Because we precisely recovered V_p^{um} and V_p^{lc}, the synthetic *SsPmp* matches the observation almost perfectly (Fig. 4b). For the same 'observed' data ($p = 0.128$ s km^{-1}), when we vary V_p^{lc} from the true value to 6.2 and 6.8 km s^{-1} ($\sim\pm5$ per cent perturbation), only $\sim\pm0.6$ per cent error is introduced in estimated V_p^{um} ($<\pm0.05$ km s^{-1}), and its effect on estimated Moho depth is negligible (Fig. 4c). The misfit curves for $V_p^{lc} = 6.2$, 6.5 and 6.8 km s^{-1} have very similar minima, indicating that the synthetics fit the 'observed' data equally well for all three cases (Fig. 4d). Because Φ_{VDSS} is matched precisely in all three cases, the correct T_{VDSS} is found in each case and we are able to give the correct CMB depth despite errors in assumed V_p^{lc} (Fig. 4c). However, when $p = 0.136$ s km^{-1}, again varying V_p^{lc} from 6.2 to 6.8 km s^{-1} causes $\sim\pm1$–2 per cent error in the estimated V_p^{um}, significantly larger than for $p = 0.128$ s km^{-1}, though the effect on estimated Moho depth remains negligible (Fig. 4e) due to precise matching of the *SsPmp* waveforms. We also observe that the troughs of the misfit curves are significantly wider for $p = 0.136$ s km^{-1} than for $p = 0.128$ s km^{-1}, indicating poorer constraints on V_p^{um} (Fig. 4f). These results show that, in a 1-D earth, matching Φ_{VDSS} alone is sufficient to estimate T_{VDSS} and Moho depth precisely, whereas to infer V_p^{um} from Φ_{VDSS} requires a priori knowledge of V_p^{lc}. If V_p^{lc} is poorly constrained in the study region, it is better to use *SsPmp* waveforms with $1/p$ close to V_p^{um}, so that an incorrectly assumed V_p^{lc} causes less error in the estimated V_p^{um}. Even in cases with well-constrained V_p^{lc}, using *SsPmp* waveforms with $1/p$ close to V_p^{um} is still preferred because the narrower troughs of the misfit curves in such cases would result in better constrained V_p^{um} (smaller uncertainty; Supplementary Text 1).

Because in field data the *S* wave trains are usually contaminated by *P*-wave coda, it is important to test our methods for cases with reasonable noise level. To simulate realistic noise, we generate Gaussian white noise, bandpass filter it between 0.05 and 0.5 Hz (a range typically used for filtering field data) and scale the noise

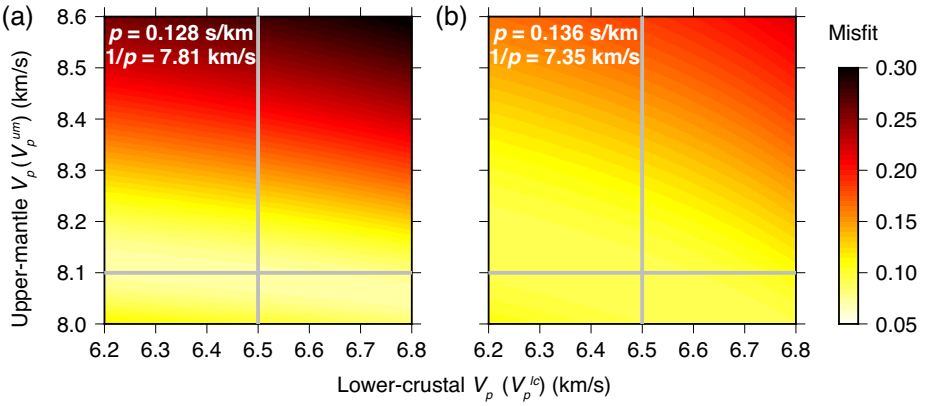

Figure 3. Normalized misfit between synthetic waveforms generated with a grid search in V_p^{um}-V_p^{lc} space and 'observed waveform' computed with Model #1 for (a) $p = 0.128$ s km^{-1} and (b) $p = 0.136$ s km^{-1}. Best fit to the 'observed waveform' is always at the Model #1 parameters (gray crosses), but V_p^{um} is most tightly constrained when the 'observed waveform' has $1/p$ close to the true V_p^{um} (from Model #1), that is far better for (a) $p = 0.128$ s km^{-1} (see Fig. 4d) than for (b) $p = 0.136$ s km^{-1} (see Fig. 4f).

so that its standard deviation is 10 per cent of the peak amplitude on the radial-component data. We add random noise independently to the same radial- and vertical-component synthetic waveforms used in the noise-free case (Fig. 4) and again attempt to retrieve V_p^{um} and Moho depth (Fig. S1). For $p = 0.128$ s km^{-1}, the derived V_p^{um} and Moho depth are significantly biased due to the interference of noise with the *SsPmp* waveform (Figs S1a–d), whereas the two parameters are reasonably well-recovered for the case with $p = 0.136$ s km^{-1} (Figs S1e and f). Since the added noise is random, the higher bias for the $p = 0.128$ s km^{-1} case is likely a coincidence (noise level happens to be higher in the time window of *SsPmp*). To demonstrate this, we generate 100 random simulations of noisy *SsPmp* both for $p = 0.128$ s km^{-1} and for $p = 0.136$ s km^{-1} and derive V_p^{um} from each simulation (Fig. S2). The mean estimated V_p^{um} from 100 simulations (equivalent to 100 earthquakes with the same p recorded at a single station) are consistent with the true value both for $p = 0.128$ s km^{-1} and for $p = 0.136$ s km^{-1}, even though individual simulations (single earthquakes) can produce significant errors (Fig. S2). Therefore, the larger error for $p = 0.128$ s km^{-1} in Fig. S1 is indeed coincidental. Estimated V_p^{um} has a larger standard deviation for $p = 0.136$ s km^{-1} than for $p = 0.128$ s km^{-1} (Fig. S2) due to higher sensitivity of $\Phi_{VDSS}$to V_p^{um} when $p = 0.128$ s km^{-1} (Figs 4 and S1). In order to avoid these errors due to random noise, an obvious strategy is to combine observations of post-critical *SsPmp* from multiple events in our estimation of Moho depth and V_p^{um}.

2.3 Crustal and mantle properties from T_{VDSS} and Φ_{VDSS} of multiple events

To incorporate observations of multiple events, we first measure T_{VDSS} and $\Phi_{VDSS}$from individual events and then estimate crustal and mantle properties by modeling the observed T_{VDSS} and Φ_{VDSS}. In order to measure $T_{VDSS}$and Φ_{VDSS} simultaneously, for each event we use a cosine-tapered 15-s window around the *Ss* waveform on the S component as the source wavelet of that event. We then apply phase shifts from 0–360° to the source wavelet to create synthetic *SsPmp* waveforms with all possible phase shifts. We use cross-correlation to find the best alignment between each synthetic *SsPmp* wavelet and the observed *SsPmp*. We then normalize observed and synthetic *SsPmp* and compute the misfit between them. $\Phi_{VDSS}$is determined as the phase shift that minimizes the misfit between the synthetic and modeled *SsPmp*. We estimate the uncertainty of T_{VDSS} and Φ_{VDSS} from the curvature of the misfit-phase-shift function around Φ_{VDSS}(Text S1 and Fig. S3). We then find T_{VDSS} of each event by cross-correlation between the best-fit synthetic *SsPmp* and the observed *SsPmp*. After measuring T_{VDSS} and Φ_{VDSS} for all events, we use the two parameters as functions of ray parameters to constrain crustal and mantle properties. Following Kang *et al*. (2016), we use T_{VDSS} as a function of p (the moveout of post-critical *SsPmp*) to constrain V_p^{av} and Moho depth H with linear regression, which also gives uncertainties of estimated V_p^{av} and H (Fig. 5c). In our linear regression procedure, we scale each data point with its uncertainty, so that data points with high uncertainty have smaller weight on the results. To constrain V_p^{um}, we compare observed Φ_{VDSS} as a function of p with theoretical Φ_{VDSS}-p relations computed with a fixed V_p^{lc} and a range of V_p^{um} (Fig. 5d).

To test our method, we generate synthetic *SsPmp* waveforms using Model #1 and $p = 0.124$–0.134 s km^{-1}, on which we can clearly observe a decrease in T_{VDSS} and Φ_{VDSS} with increasing p (Fig. 5a). We then measure T_{VDSS} and Φ_{VDSS} from the observed *SsPmp* of each event, an example of which is shown in Fig. 5(b). The observed T_{VDSS}-p relation gives a best-fitting $V_p^{av} = 6.5 \pm 0.1$ km s^{-1} and $H = 40 \pm 1$ km, in good agreement with the input model (Fig. 5c). To find the best-fitting V_p^{um}, we plot theoretical Φ_{VDSS}-p relations with different V_p^{um} values while assuming $V_p^{lc} = 6.5$ km s^{-1}, the true V_p^{lc}, and compare them with the observed values. The comparison shows that the observations favour $V_p^{um} = 8.1$ km s^{-1}, consistent with the input model (Fig. 5d). To test the effects of assumed V_p^{lc} on the estimated V_p^{um}, we compare theoretical curves computed assuming $V_p^{lc} = 6.2, 6.5, 6.8$ km s^{-1} (∼5 per cent perturbation; Fig. 6). For $V_p^{lc} = 6.2$ and 6.8 km s^{-1}, the theoretical Φ_{VDSS}-p curves overlap when p is small and gradually diverge as p increases (Fig. 6), but never to the extent that would significantly affect the estimated V_p^{um} (Fig. 6). The theoretical Φ_{VDSS}-p relations are insensitive to assumed V_p^{lc} because the reciprocal of ray parameter ($1/p$) considered here (7.5–8.1 km s^{-1}) is significantly higher than the assumed V_p^{lc}, which makes Φ_{VDSS} insensitive to V_p^{lc} (Fig. 7a in Part 1). In the case of $V_p^{lc} = 6.2$ km s^{-1} (6.8 km s^{-1}), the theoretical Φ_{VDSS}-p curves are shifted slightly upward (downward) compared with $V_p^{lc} = 6.5$ km s^{-1}, because for a fixed p, decreasing (increasing) V_p^{lc} while fixing Φ_{VDSS} requires an increase (decrease) in V_p^{um} (negative trade-off between V_p^{lc} and V_p^{um}; Fig. 7 in Part 1).

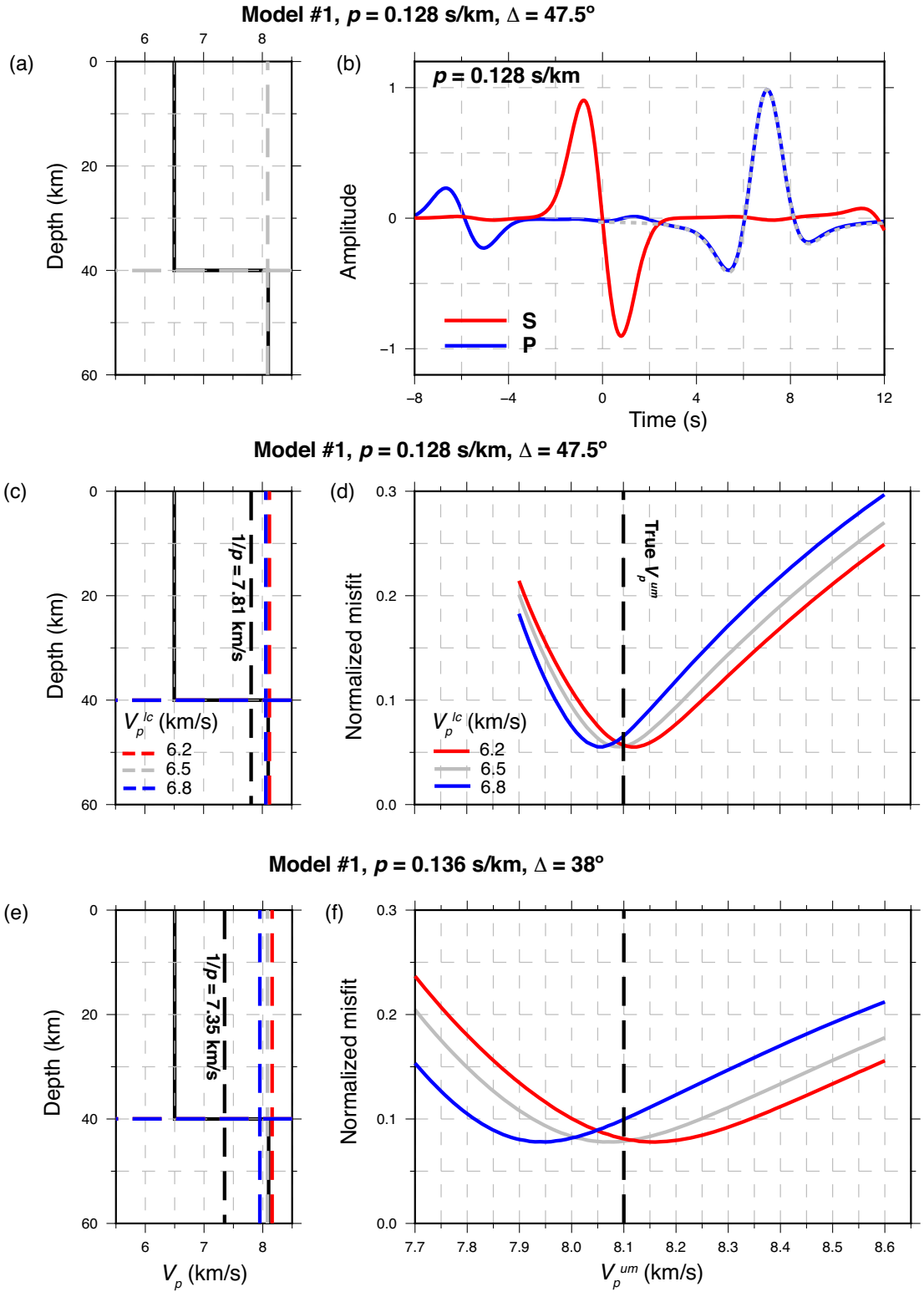

Figure 4. Estimating Moho depth and V_p^{um} from waveforms computed for Model #1 with an assumed V_p^{lc}. (a) and (b) Moho depth and V_p^{um} derived using the correct $V_p^{lc} = 6.5$ km s^{-1}. (a) Gray dashed lines: Moho depth and V_p^{um} that best fit T_{VDSS} and Φ_{VDSS}, very closely matching Model #1 (black line). $V_p^{av} = 6.5$ km s^{-1} is used to convert T_{VDSS} to Moho depth. (b) Synthetic *P* and *S* waveforms computed for Model #1 and $p = 0.128$ s km^{-1} ('observations'). Grey dashed curve: *P*-component *SsPmp* waveform that best fits T_{VDSS} and Φ_{VDSS}. (c–f) A comparison of results derived with different assumed V_p^{lc}. (c) and (e) Model #1 as in (a) with Moho depths and V_p^{um} estimated for assumed $V_p^{lc} = 6.2$ (red), 6.5 (grey) and 6.8 (blue) km s^{-1}, for $p = 0.128$ and 0.136 s km^{-1} respectively. Black dashed lines mark the critical velocities ($1/p$) in the two cases. (d) and (f) Normalized misfits as functions of V_p^{um} for each case. Note the choice of V_p^{lc} has little effect on estimated V_p^{um} when p is small ($1/p$ is large and close to V_p^{um}), but has a significant effect when p is large ($1/p$ is small and far from V_p^{um}).

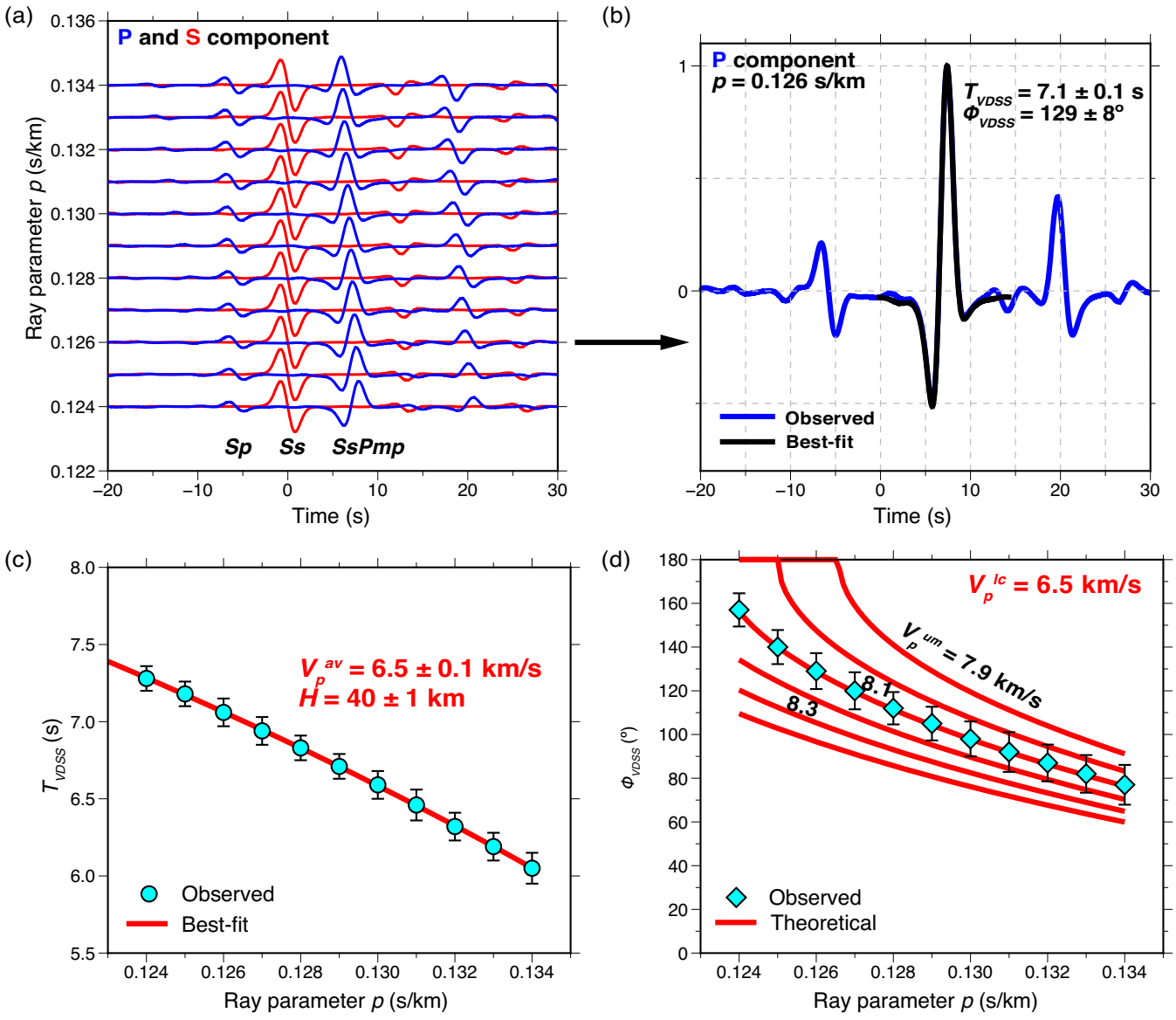

Figure 5. Synthetic example of constraining crustal and upper mantle properties with *SsPmp* of multiple events observed at a single station. (a) *P* and *S*-component synthetic waveforms for events with $0.124 \leq p \leq 0.134$ s km^{-1}. Black arrow marks the event shown in (b). Note that T_{VDSS} decreases with increasing p. (b) Observed and best-fitting *P*-component waveforms for the event with $p = 0.126$ s km^{-1}. (c) Observed and best-fit T_{VDSS} as functions of ray parameter from linear regression (Kang *et al*. 2016). Note V_p^{av} and H are both recovered well. (d) Observed and theoretical relations between Φ_{VDSS} and ray parameter for variable V_p^{um} but V_p^{lc} fixed at 6.5 km s^{-1}. Note V_p^{um} is well-recovered.

We also test our multi-event method using noisy synthetic data. We contaminate our synthetic data with the same 10 per cent band-limited white noise as described before (Fig. S4a). Whereas *SsPmp* is clearly observed despite the addition of noise, *Sp*, the phase used in *S* receiver functions, is barely observable (Fig. S4a). We then process the noisy synthetic waveforms as described above. The measured T_{VDSS} and Φ_{VDSS} have significantly higher uncertainties compared to the noise-free case (0.2 s versus 0.1 s and 14° versus 8° for the event with $p = 0.126$ s km^{-1}; Fig. S4b). Nonetheless, our method still yields V_p^{av} and H that agree reasonably well with the input model (6.4 ± 0.2 km s^{-1} versus 6.5 km s^{-1} and 38 ± 3 km versus 40 km; Fig. S4c). The observed Φ_{VDSS}-p relation also favours $V_p^{\mathrm{um}} = 8.1 \pm 0.1$ km s^{-1} despite scattering of the data points (Fig. S4d). In short, we show that our proposed multi-event analysis can robustly retrieve V_p^{av}, H and V_p^{um} from data with moderate noise levels, making it suitable for application to field data.

2.4 Average crustal V_p/V_s ratio (κ) and composition from joint PRF-VDSS analysis

Because rock V_p/V_s ratios are sensitive to rock composition (Christensen 1996), estimation of average crustal V_p/V_s ratio (also denoted κ) can offer insights into bulk composition of the crust, thus tectonic evolution of the area. Conventionally, κ has been estimated using the H–κ method, which searches for the model that maximizes the stacked energy of Moho *Ps* and multiples on PRFs (*PpPms*, *PpSms*, etc.; Zhu & Kanamori 2000). However, the conventional H–κ method has two major disadvantages. First, it uses the Moho multiples on PRF, which are not always robustly observed. Secondly,

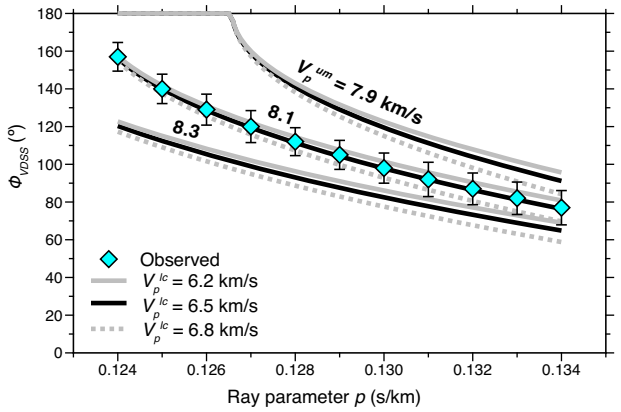

Figure 6. Effects of assumed V_p^{lc} on V_p^{um} derived from observed Φ_{VDSS} as a function of ray parameter. The black curves ($V_p^{lc} = 6.5$ km s^{-1}) and data points are the same as the ones in Fig. 5(d).

it requires V_p^{av} as an input parameter, which needs to be estimated independently. A recent proposal to complement conventional H–κ method with *SsPmp* observations in order to estimate V_p^{av} still requires robust observation of at least one Moho multiples on PRFs (Luo *et al*. 2018). Here, we present a joint PRF-VDSS analysis method to derive κ without this limitation by using the moveout of *SsPmp* to constrain V_p^{av} and H.

With a 1-D assumption, the arrival time of the Moho *Ps* in PRF can be expressed as:

$$T_{Ps} = H\left(\sqrt{\left(\frac{k}{V_p^{av}}\right)^2 - p^2} - \sqrt{\left(\frac{1}{V_p^{av}}\right)^2 - p^2}\right) \quad (2)$$

Using H (hereafter H_{VDSS}) and V_p^{av} given by *SsPmp* observations, we can derive κ (hereafter κ_{joint}) from T_{Ps} (Fig. 7). To estimate the uncertainty of our κ_{joint}, we draw 5000 random samples of V_p^{av} and H_{VDSS} from their joint distribution (Kang *et al*. 2016) and compute κ_{joint} for each pair. We then estimate uncertainty of our κ_{joint} from the variance of the 5000 randomly simulated κ_{joint} (Fig. 7). Since V_p^{av} and κ_{joint} together place key constraints on average crustal composition (Christensen & Mooney 1995; Christensen 1996), we also compute the joint distribution of V_p^{av} and κ_{joint} and compare them with laboratory measurements (Fig. 8).

We again use synthetic data to test our method. We generate synthetic PRFs using Model #1, apply normal moveout, and stack them. From the stacked PRF, the Moho $T_{Ps}$is picked at 4.50 s (Fig. 7a). Using our T_{Ps} and the previously estimated $V_p^{av} = 6.5 \pm 0.1$ km s^{-1} and $H_{VDSS} = 40 \pm 1$ km, we find $\kappa_{joint} = 1.73 \pm 0.02$ (Fig. 7b), consistent with the input model. We also plot the joint distribution of V_p^{av} and κ_{joint}, which shows a clear negative correlation between the two parameters (Fig. 8). To compare our seismic 'observations' with laboratory measurements, we plot V_p and κ of major crustal rock types measured at 600 MPa (corresponds to mid-crustal depth) and room temperature from Christensen (1996, Fig. 8). We also plot V_p, κ and SiO_2 content of individual samples (excluding eclogites and ultramafic rocks) measured at 600 MPa and room temperature (compilation of Hacker *et al*. 2015). For typical crustal rocks, $dV_p/dT = \sim -0.4$ m s^{-1} °C^{-1}, and $dV_s/dT = \sim -0.2$ m s^{-1} °C^{-1}, so typical $d\kappa/dT = \sim -0.0015/100$ °C (Christensen & Mooney 1995; Barruol & Kern 1996; Christensen 1996). With these relations, we apply temperature corrections to the measurements from Christensen (1996) and Hacker *et al*. (2015) assuming a mid-crustal temperature of ∼250°, suitable for cratonic crust. We note that the temperature correction (−0.1 km s^{-1}) is moderate for V_p, but negligible (−0.004) for κ, indicating that κ is primarily controlled by rock composition (Christensen 1996). The laboratory measurements show a clear correlation of increasing V_p and κ with decreasing SiO_2 content (Fig. 8). Because our V_p-κ correlation from VDSS-PRF analysis is orthogonal to the V_p-κ correlation of laboratory measurements, our method constrains the average crustal composition in this synthetic example as intermediate (equivalent to diorite or felsic granulite, Fig. 8). We recognize the large scatter of individual laboratory measurements of similar composition (coloured circles; Hacker *et al*. 2015) and the large variation between aggregated samples that share the same rock name (diamonds; Christensen 1996) around the positive V_p-κ trend, but note that these compilations represent samples collected in highly diverse geological settings. When applying our method to a specific region, a more desirable approach would be to build a rock physics model appropriate for that region.

3 OBSERVATIONS AND INTERPRETATIONS OF THE SOUTHWEST SLAVE CRATON

The Canadian Shield has a longevity and stability suggestive of a lithospheric structure closer to 1-D than tectonically active areas. The Yellowknife Array was deployed in the Slave Craton of the Canadian Shield (Figs 9a and b) in 1962 and was upgraded to digital recording in 1989 (Bostock 1998). The long deployment time and its location at the core of the Canadian Shield makes it an ideal place to test our proposed method for retrieving and analysing both T_{VDSS} and Φ_{VDSS} under a 1-D assumption. In addition, the LITHOPROBE project acquired wide-angle refraction and near-vertical reflection profiles through Yellowknife (Fernández-Viejo & Clowes 2003; Fernández-Viejo *et al*. 2005; Hammer *et al*. 2010), allowing direct comparison between VDSS and active-source results.

3.1 VDSS and PRF data analysis

Among stations of the Yellowknife Array, YKW3 has the longest archived broadband recording (1994–2014). In addition, Station EDZN of the POLARIS array (Snyder & Bruneton 2007) was located ∼80 km NW of YKW3, within ∼25 km of *SsPmp* Moho reflection points for Kamchatka-Kurile earthquakes recorded at YKW3 (Fig. 9b), allowing us to compare PRF results at EDZN with VDSS results at YKW3, as conversion points of PRFs at Moho depth are typically <20 km away from the station. For VDSS analysis at YKW3, we examined 56 teleseismic events in the epicentral range 30–60° with the back-azimuth range of 290–310°. We choose this narrow backazimuth range to avoid possible complications from lateral variation in lithospheric structure [the Moho reflection points of our selected events are all within 25 km of each other (Fig. 9b)], while still including plenty of events from the Kamchatka subduction zone with a wide range of ray parameters (Figs 9a and c). We removed instrumental response and applied a bandpass Butterworth filter between 0.05 and 0.5 Hz. After separating radial and vertical-component data into *P* and *S* components, we inspected the traces and their particle-motion diagrams, selecting the 19 events with simple *Ss* waveforms and significant *P* energy following the *S* arrival. We next computed the envelope functions of the *P* and *S* components of the 19 events and rejected the nine 'Grade C' events for which the ratio of the maxima of the *P* and *S* envelope functions ≤0.6. The remaining 10 events all have simple *Ss* waveforms and

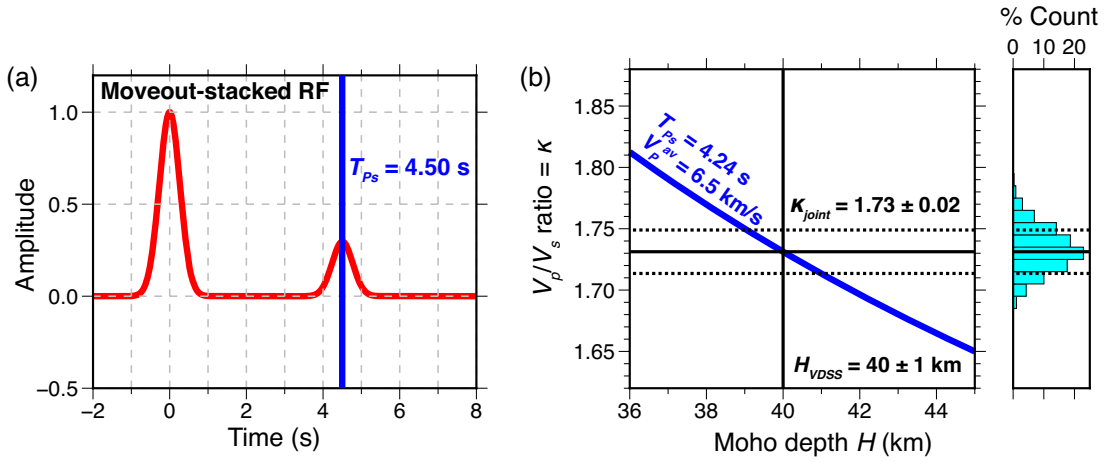

Figure 7. Synthetic example of constraining average crustal V_p/V_s ratio (κ) via PRF-VDSS joint analysis. (a) Synthetic PRF computed with Model #1, after moveout-correction to normal incidence. (b) Determination of crustal average V_p/V_s ratio (κ_{joint}) from PRF T_{Ps}, VDSS Moho depth (H_{VDSS}), and VDSS average crustal V_p(V_p^{av}). Dashed black lines mark the estimated uncertainty of κ_{joint}, which is computed by taking the standard deviation of 5000 random simulations of κ_{joint} (cyan histogram). Note κ is well recovered.

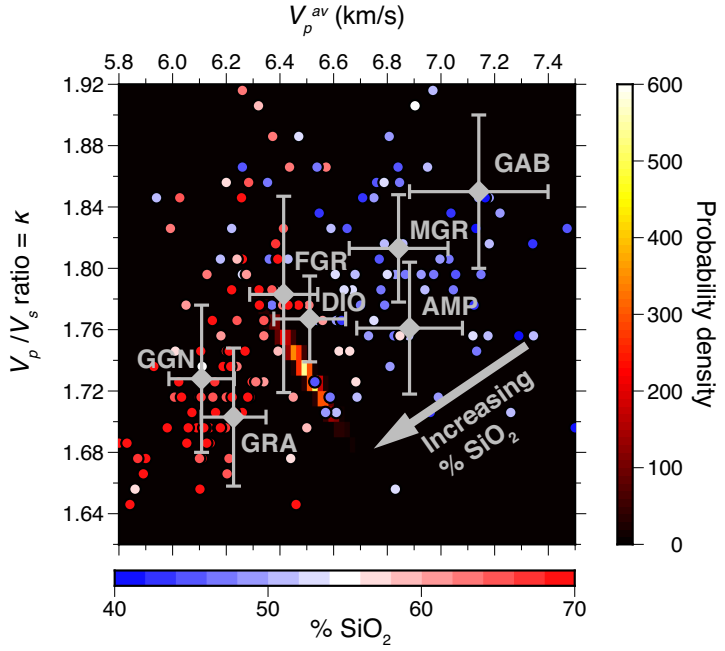

Figure 8. Synthetic example of constraining average crustal composition with PRF-VDSS joint analysis. The probability density function is derived from 5000 random simulations of V_p^{av} and κ. Circles coloured by per cent SiO_2 are measurements for crustal rock samples (felsic to mafic) at 600 MPa and room temperature (compilation of Hacker *et al*. 2015), which are then corrected to 250 °C (see Section 2.4). Gray diamonds and data ranges are measurements at 600 MPa and room temperature from Christensen (1996), which are also corrected to 250 °C. GAB: Gabbro-norite-troctolite; MGR: Mafic granulite; DIO: Diorite; FGR: Felsic granulite; GGN: Granite gneiss; GRA: Granite-granodiorite; AMP: Amphibolite. Note the orthogonal trends of the probability density function and per cent SiO_2, which constrains average crustal composition.

strong *SsPmp* following the *Ss* arrival (Fig. 9c). When sorted by their ray parameter, the 10 traces show a clear decrease of T_{VDSS} (moveout) with increasing ray parameter (Fig. 9c). To measure T_{VDSS} and Φ_{VDSS}, we used a 20 s-window around *Ss* as our source wavelet to account for the slightly lower frequency of the observed data compared with our synthetics. After measuring T_{VDSS} and Φ_{VDSS}, we excluded three 'Grade B' events with minimum misfit >0.4, because their large misfit implies that *SsPmp* is poorly approximated by a phase-shifted source time function, violating a basic assumption. We used measured T_{VDSS} and Φ_{VDSS} of the remaining seven 'Grade A' to derive $V_p^{av} = 6.7 \pm 0.2$ km s^{-1}, $H = 38 \pm 4$ km (Fig. 9e) and $V_p^{um} = \sim 8.0$–8.1 km s^{-1} (Fig. 9f) as described above.

For PRF analysis at EDZN, we used a time-domain iterative deconvolution algorithm with a Gaussian bandwidth of 2.5 Hz (Herrmann 2013) to compute PRFs for teleseismic *P*-wave data from 30–90° (Fig. S5). We manually selected 73 high-quality radial RFs using the Funclab software package (Porritt & Miller 2018), moveout-corrected the RFs to normal incidence for primary *Ps* conversions and stacked, which yields a clear Moho *Ps* at 4.24 s and little energy from intra-crustal converters (Fig. 10a). Using

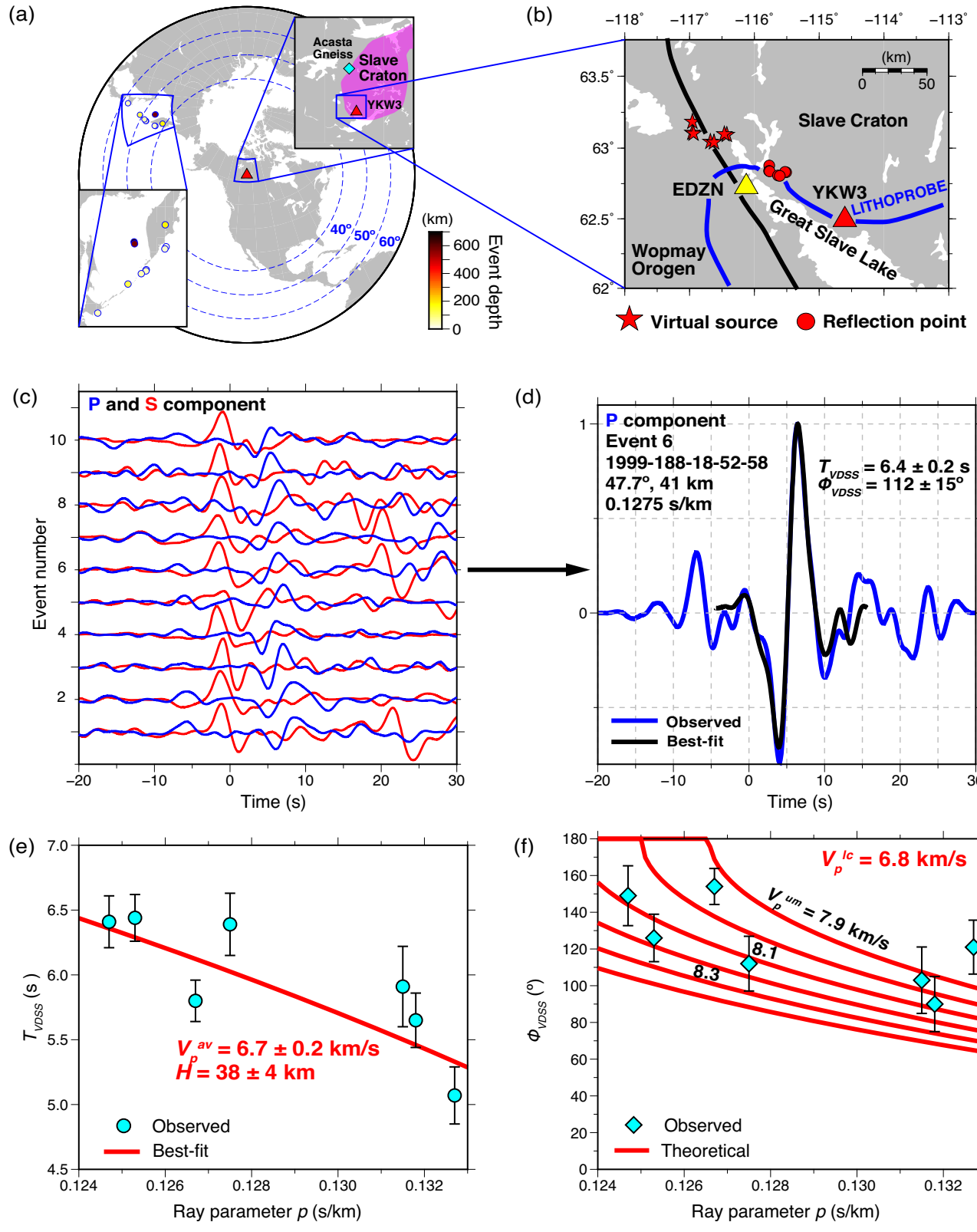

Figure 9. V_p^{um}, V_p^{av} and Moho depth H near station YKW3 derived from T_{VDSS} and Φ_{VDSS}. (a) Station and event distribution on a polar plot centered on YKW3. 10 Grade A and B events with backazimuth 297–304°, M_w > 5.5, distance 40–60° and depth 30–700 km, are coloured by their focal depth. (b) Locations of broadband stations YKW3 and EDZN (triangles), LITHOPROBE reflection and refraction profiles (blue line), and VDSS Moho reflection points and virtual sources. The reflection-point and virtual-source locations are computed using the best-fitting V_p^{av} and H (part e) for the seven Grade A events (part c). PRF results for EDZN are shown in Figs. 10 and S5. (c) *P*- and *S*-component waveforms of the ten Grade A and B events. Events are sorted by their ray parameters (small to large), with detail information in Table S1. Black arrow marks Event 6 shown in (d). (d) Observed and best-fitting *P*-component waveforms of Event 6. (e) Observed T_{VDSS} as functions of ray parameter and the best-fitting model from linear regression. (f) Observed and theoretical relations between Φ_{VDSS} and ray parameter for variable V_p^{um} but V_p^{lc} fixed at 6.8 km s^{-1}. The observations favour V_p^{um} ~8.0–8.1 km s^{-1}.

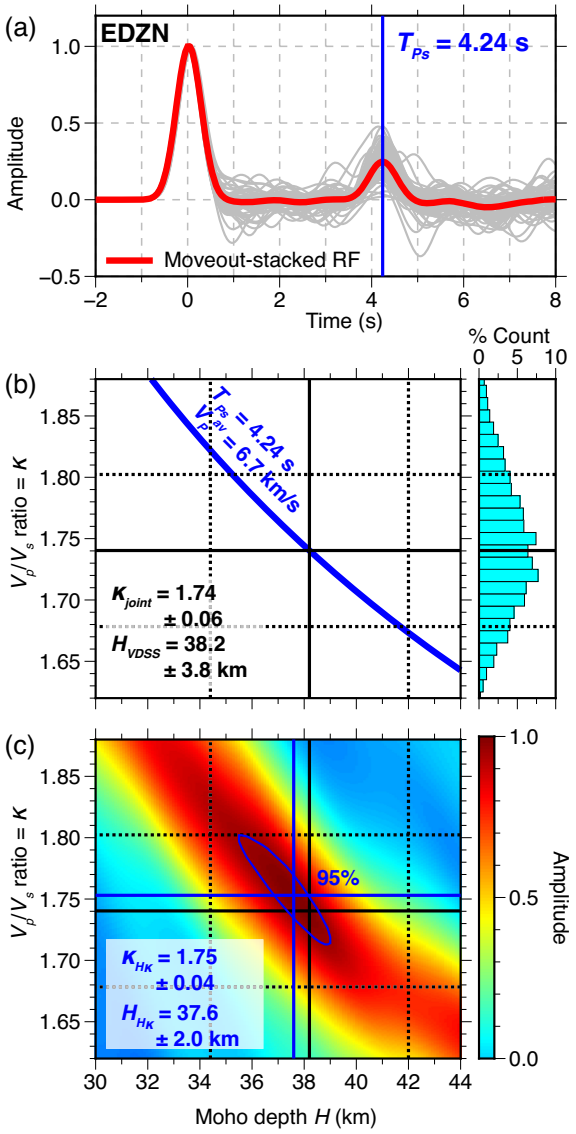

Figure 10. PRF-VDSS joint analysis for crustal structure of the SW Slave Craton. (a) PRF waveforms of EDZN. The stacked PRF is computed by summing 73 PRFs (grey curves) moveout-corrected to normal incidence. (b) Determination of average crustal V_p/V_s ratio (κ_{joint}) from PRF T_{Ps}, VDSS Moho depth ($H_{\rm VDSS}$), and average crustal V_p($V_p^{\rm av}$). The dashed black lines mark the uncertainties of κ_{joint}, which is computed by taking the standard deviation of 5000 random simulations of κ_{joint} (cyan histogram). (c) Comparison between $H_{\rm VDSS}$ and κ_{joint} and H and κ derived from conventional H–κ stacking ($H_{H\kappa}$ and $\kappa_{H\kappa}$). Background colour is normalized amplitude of the conventional H–κ stack computed with $V_p^{\rm av}$ = 6.7 km s^{-1} and phase weight ratios w_{Ps}:w_{PpPms}:w_{PpSms} = 1:0.5:0.5. The >95 per cent amplitude range is outlined in blue, from which the uncertainty of $H_{H\kappa}$ and $\kappa_{H\kappa}$ are estimated. Note H and κ derived with the two methods are very close (<1 per cent difference), whereas the uncertainties are on the same order of magnitude.

T_{Ps}measured from our moveout-stacked PRFs and H and $V_p^{\rm av}$ from our VDSS analysis, we estimate κ_{joint} = 1.74 ± 0.06 (Fig. 10b). We also performed conventional H-κ stacking of our 73 selected RFs using a phase weight ratio w_{Ps}:w_{PpPms}:w_{PpSms} = 1:0.5:0.5 (Zhu & Kanamori 2000) and $V_p^{\rm av}$ = 6.7 km s^{-1} taken from our VDSS analysis to determine $H_{H\kappa}$ = 37.6 km and $\kappa_{H\kappa}$ = 1.75 (Fig. 10c). We estimate the uncertainties of $H_{H\kappa}$ and $\kappa_{H\kappa}$ (± 2.0 km and ± 0.04, respectively) using the range with stacking amplitude > 95 per cent of the peak value while ignoring the additional uncertainties arising from the choice of $V_p^{\rm av}$ and phase stacking weights (supplementary figures in Karplus *et al*. 2019).

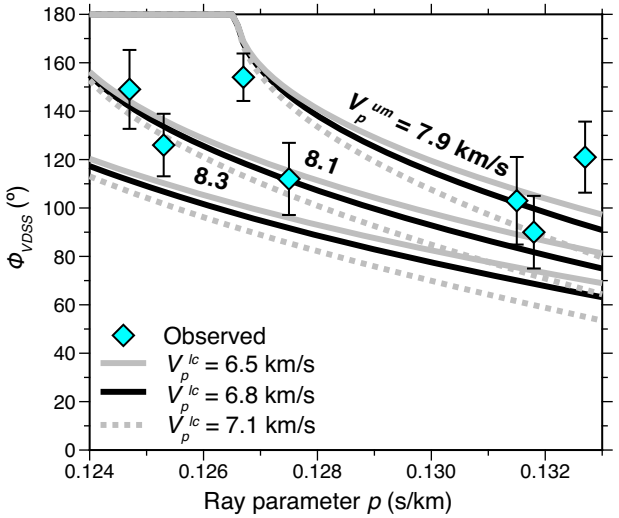

Figure 11. Effects of assumed $V_p^{\rm lc}$ on $V_p^{\rm um}$ derived from observed $\Phi_{\rm VDSS}$ as a function of ray parameter at YKW3. The black curves ($V_p^{\rm lc}$ = 6.8 km s^{-1}) and observations (data points) are the same as the ones in Fig. 9(f).

We also computed transverse PRFs. We found neither azimuthal variation of Moho *Ps* on the radial PRFs (Figs S5b and c) nor clear Moho *Ps* on the transverse PRFs (Figs S5d and e), indicating negligible Moho dip or crustal anisotropy. We do however observe a coherent negative arrival at ∼8 s on the transverse PRFs (Figs S5d and e), which may correspond to the intra-mantle 'H converter' imaged beneath Yellowknife by Bostock (1998).

3.2 Uncertainties and sensitivities of VDSS analyses

The observed $T_{\rm VDSS}$ of Grade A events clearly decreases with increasing ray parameter, with a typical uncertainty of ±0.3 s (Fig. 9e). We find the best-fitting crustal $V_p^{\rm av}$ and Moho depth ($H_{\rm VDSS}$) to be 6.7 ± 0.2 km s^{-1} and 38 ± 4 km, respectively (Fig. 9e). The observed $\Phi_{\rm VDSS}$ of Grade A events also shows a clear decrease with increasing ray parameter (Fig. 9f), in accord with our theoretical predictions (Part. 1). To find the best-fitting $V_p^{\rm um}$, we plot theoretical $\Phi_{\rm VDSS}$-p relations for different $V_p^{\rm um}$ values while fixing $V_p^{\rm lc}$ = 6.8 km s^{-1}, the value given by wide-angle refraction studies close to our VDSS reflection points (Fig. 9f, Fernández-Viejo & Clowes 2003). Comparing our observed values with the theoretical relations, we find that the observations favour $V_p^{\rm um}$ = 8.0–8.1 km s^{-1}, consistent with the *Pn* velocity of 8.2 ± 0.1–0.2 km s^{-1} reported by the wide-angle refraction studies (Fernández-Viejo & Clowes 2003; Fernández-Viejo *et al*. 2005). Our choice of $V_p^{\rm lc}$ has little effect on estimated $V_p^{\rm um}$ given the ∼20° uncertainty in observed $\Phi_{\rm VDSS}$, as shown by theoretical curves computed assuming $V_p^{\rm lc}$ = 6.5, 6.8 and 7.1 km s^{-1} (∼4 per cent perturbation) (Fig. 11). This is because the range of 1/p considered here (7.5–8.0 km s^{-1}) is significantly higher than the assumed $V_p^{\rm lc}$, making $\Phi_{\rm VDSS}$ insensitive to $V_p^{\rm lc}$ (Fig. 7 in Part 1).

In addition to using only our seven Grade A events, we test the effects of also including Grade B and C events, which gives significantly higher values for $V_p^{\rm av}$ and H (Fig. S6a). This increase in $V_p^{\rm av}$and H is primarily due to the large $T_{\rm VDSS}$of Grade B and C events with small ray parameter (Fig. S6a). Similarly, inclusion of

Grade B and C events significantly increases our estimate of V_p^{um} (Fig. S6b). This increase in V_p^{av}, H and V_p^{um} is primarily due to most of the Grade B and C events coincidentally having smaller ray parameters than Grade A events, even though our data selection was not based on ray parameter. For events with $p < 0.122$ s km^{-1}, the turning velocity $1/p$ of the downgoing P wave exceeds 8.2 km s^{-1}, higher than the velocity we estimated for the top of the upper mantle ($V_p^{um} = 8.1$–8.0 km s^{-1}). Therefore, *SsPmp* with $p < 0.122$ s km^{-1} has turned or been refracted within the upper mantle below the CMB. These events thus likely provide estimates of V_p^{um} more appropriate for the depth at which the rays turn, and estimates of V_p^{av} and H that average the crust and upper mantle. Previous wide-angle refraction results suggested that V_p increases from 8.2 km s^{-1} right below the Moho to 8.5 km s^{-1} at ∼65 km depth between YKW3 and EDZN (Fernández-Viejo & Clowes 2003), consistent with our observation that Φ_{VDSS}at low ray parameter suggests $V_p^{um} = 8.4$–8.6 km s^{-1} (Fig. S6b). Additional difficulties may arise if the turning velocity is only slightly higher than the velocity just below a sharp CMB, because strong pre-critical reflections at the CMB will interfere with *SsPmp* that turns in the upper mantle (Fig. 5 in Part 1), causing a complicated *SsPmp* waveform that cannot be modeled with a phase-shifted S wavelet. Moreover, as p decreases and *SsPmp* becomes a turning wave in the upper mantle, the distance between the virtual source and station grows, increasing the effects of lateral heterogeneity on T_{VDSS} and Φ_{VDSS}. These complications may cause the large uncertainty and scatter of measured T_{VDSS} and Φ_{VDSS} for events with small p (Fig. S6). In summary, when constraining V_p^{av} and H with T_{VDSS}, it is appropriate to only use events with $1/p$ smaller than V_p^{um}, because the behaviour of *SsPmp* as an upper-mantle turning wave is more complicated than modelled here. Nonetheless, this behaviour may open the way to continuous depth profiling of upper-mantle velocity structure in future work.

3.3 Comparison with previous imaging and geologic interpretations

Our Moho depth ($H_{VDSS} = 38 \pm 4$ km, Fig. 9e) is in good agreement with LITHOPROBE near-vertical reflection results (∼37 km), but slightly deeper than their seismic refraction results (∼31–33 km, Fernández-Viejo *et al*. 2005; Hammer *et al*. 2010, Fig. 12). Our average crustal V_p ($V_p^{av} = 6.7 \pm 0.2$ km s^{-1}, Fig. 9e) is also higher than the value given by the wide-angle refraction studies (∼6.4 km s^{-1}, Fernández-Viejo *et al*. 2005; Hammer *et al*. 2010, Fig. 12). Our H_{VDSS} closely matches our H–κ Moho depth ($H_{VDSS} = 38.2 \pm 3.8$ km; $H_{H\kappa} = 37.6 \pm 2.0$ km; Fig. 10c). This agreement not only verifies our VDSS method, but also indicates that $V_p^{av} = 6.7$ km s^{-1} assumed for the H–κ analysis is likely a reliable estimation of average crustal V_p. Similarly, the agreement between $\kappa_{joint} = 1.74 \pm 0.06$ and $\kappa_{H\kappa} = 1.75 \pm 0.04$ (Fig. 10) further demonstrates the robustness of our method, though our κ values are higher than those from the refraction study that found $\kappa = 1.68$–1.72 in the Slave Craton (Fernández-Viejo *et al*. 2005).

Our joint distribution between $V_p^{av}$and κ_{joint} shows a clear negative correlation (Fig. 13), similar to our synthetic example (Fig. 8), though the field data is less focused than the synthetics due to larger observation uncertainty. We again compare the joint distribution with the temperature-corrected laboratory measurements from Christensen (1996) and Hacker *et al*. (2015), which implies an intermediate (dioritic) average crustal composition, though some mafic rock samples also fit our preferred V_p^{av}-κ estimates (Fig. 13). The refraction $V_p^{av}$and κ values (Fernández-Viejo *et al*. 2005) are quite distinct (green ellipse in Fig. 13) and imply a felsic (granitic) average crustal composition.

Fernández-Viejo *et al*. (2005) interpreted their low average $V_p^{av}$and κ as evidence for a 'significant felsic content' of the crust in the SW Slave Craton and explained the regional Bouguer gravity low with their silicic but thin crust. Our more-mafic but thicker crust could equally match the gravity signature. We also note that the lower V_p^{av} and thinner crust found by wide-angle refraction experiments could partly be explained by a positive trade-off between the two parameters.

The Slave craton is home to the Earth's oldest rocks, the Acasta Gneiss with Hadean ages ≥4 Ga (Bowring & Williams 1999), though the bulk of its crust is clearly Archaean. In the SW Slave Craton, geochronology of surface exposures emphasizes the importance of Neoarchaean crustal growth at <2.6 Ga (Bennett *et al*. 2005), but other crustal-scale cross-sections show the Palaeoarchean-to-Mesoarchean Central Slave Basement Complex forming the bulk of the crust (Bleeker 2002), as also interpreted from LITHOPROBE near-vertical reflection profiling (van der Velden & Cook 2002). Our observation of crustal thickness, V_p^{av} and κ may help resolve the dominant crustal formation age of the SW Slave Craton. A trend of increasing V_p^{av}, κ and crustal thickness with decreasing crustal age in the Western Australia Craton has been suggested to reflect a global transition of crust-forming mechanism from plume tectonics to plate tectonics during Archean (Yuan 2015). If this relationship were to be applicable to the Canadian cratons, our results are most consistent with a Mesoarchean formation age for the bulk crust of the SW Slave Craton.

4 DISCUSSION

Post-critical *SsPmp* has three major attributes: T_{VDSS}, Φ_{VDSS} and A_{VDSS}. In 1-D, A_{VDSS} is largely affected by near-surface velocity (Fig. 10 in Part 1), whereas T_{VDSS} and Φ_{VDSS} both contain information on crustal and upper-mantle structure. In this paper, we propose methods to retrieve Moho depth, V_p^{av} and V_p^{um} from *SsPmp* observations under a 1D assumption.

$T_{VDSS}$is controlled by Moho depth and V_p^{av} and can be measured together with Φ_{VDSS} by waveform fitting (Fig. 5b). Whereas Moho depth can be estimated from a single *SsPmp* observation with an assumed V_p^{av} (Fig. 4), both H_{VDSS} and V_p^{av} can be constrained using multiple events recorded at the same station (Fig. 5) (Kang *et al*. 2016). The uncertainties of our derived H_{VDSS} and V_p^{av} at YKW3 (4 km and 0.2 km s^{-1}, respectively) are larger than those given by Kang *et al*. (2016) for two stations FORT and WB2 in Australia (∼3.0 km and ∼0.15 km s^{-1}, respectively). Two factors might contribute to the higher uncertainties of our measurements. First, the uncertainty of our T_{VDSS} (∼0.3 s) is greater than Kang et al. (∼0.18 s), but these values are not directly comparable because we compute T_{VDSS} uncertainties quantitatively (Supplementary Text 1), whereas Kang *et al*. (2016) estimated their uncertainties empirically. Second, the ray-parameter range of our study (0.1247–0.1327 s km^{-1}) is smaller than in Kang *et al*. (0.1223–0.1349 s km^{-1} for FORT and 0.1226–0.1369 s km^{-1} for WB2), largely because the number of events we used (seven) is smaller than in Kang *et al*. (20 for FORT and 12 for WB2). Our events are fewer and our ray-parameter range smaller in part due to our strict data-selection criteria (Fig. S6). In practice, the number of observations available depends on event distribution and data quality.

Φ_{VDSS} is controlled by V_p^{lc} and V_p^{um} and can be used to constrain the two parameters. Due to the trade-off between V_p^{lc} and

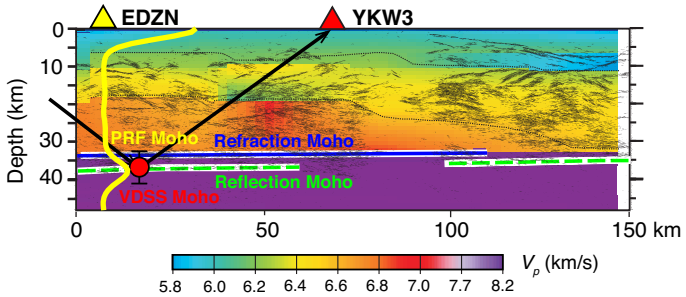

Figure 12. Comparison between our VDSS and PRF and LITHOPROBE reflection and refraction results. The migrated reflection image is overlain on the refraction V_p model (after Hammer *et al*. 2010). Red circle with error bars: VDSS Moho plotted at the reflection point; the arrows are ray paths of *SsPmp*. Yellow curve: moveout-stacked PRF mapped to depth domain and plotted at EDZN. VDSS, PRF and reflection Moho depths agree with each other (∼38 km), but the refraction Moho is shallower (∼34 km).

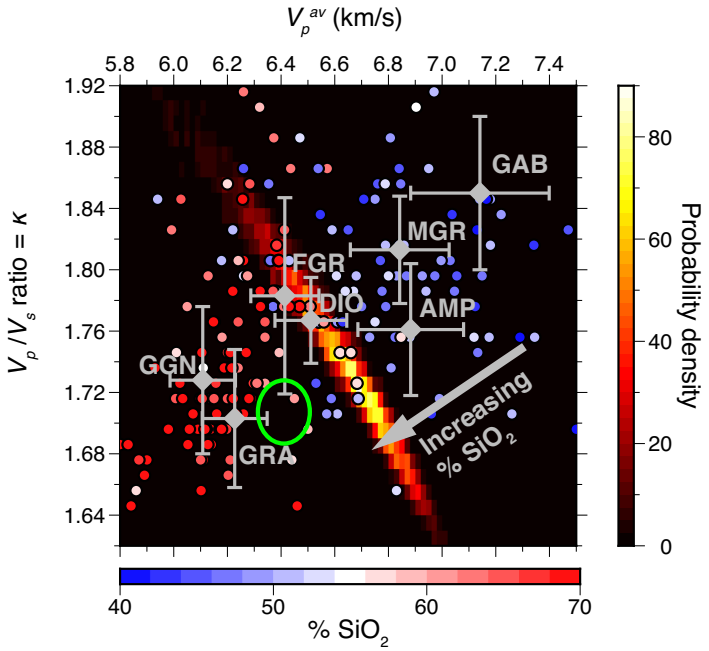

Figure 13. Average crustal composition of the SW Slave Craton constrained with PRF-VDSS joint analysis. The probability density function is derived from 5000 random simulations of V_p^{av} and V_p/V_s ratio. The diamonds and circles are the same as Fig. 8. The orthogonal trends of the probability density function and rock properties together constrain average crustal composition. Green ellipse is V_p^{av} and κ from Fernández-Viejo *et al*. (2005).

V_p^{um}(Fig. 7 in Part 1), it is impossible to determine one without knowing the other (Fig. 3). However, we show that when p is small ($1/p$ close to V_p^{um}), Φ_{VDSS} depends only weakly on V_p^{lc}, allowing determination of V_p^{um} without a precisely known V_p^{lc} (Figs 3 and 4; also Fig. 7 in Part 1). Although V_p^{um} can in principle be derived from a single *SsPmp* observation, incorporating Φ_{VDSS} from multiple events offers a more robust estimation of V_p^{um}, especially in the presence of noise (Figs 5 and S4). We note that, when measuring Φ_{VDSS}, it is important to choose traces with high signal-to-noise ratio, as waveform observables are more sensitive to noise than traveltime measurements. This is especially true when considering the higher noise level of teleseismic *S* compared to *P* wave due to coda waves generated by preceding *P* phases that arrive in the same time window. A practical criterion for data quality control is to choose *SsPmp* traces that can be well-fitted with a phase-shifted *Ss* wavelet (Fig. 9). Our field examples show that Φ_{VDSS} and T_{VDSS} of events selected this way (cyan markers in Fig. S6) in general have smaller uncertainties than the events not selected (grey markers in Fig. S6).

While inferring V_p^{um}, H_{VDSS} and V_p^{av} from Φ_{VDSS} and T_{VDSS} observations, we implicitly assume the CMB to be a sharp boundary as opposed to a broad transition zone. When the CMB is a velocity-gradient zone thinner than the dominant wave-length of the incident *P* wave (∼25 km for typical field data), as is true for most continental areas, $\Phi_{VDSS}$is not significantly different from the case with a sharp CMB (Part 1), thus our method of deriving V_p^{um} from Φ_{VDSS} still applies. When the CMB is a velocity-gradient zone with *SsPmp* rays turning within the CMB ($1/p$ in the range of the gradient-zone V_p), the T_{VDSS}-p relation (moveout) is different from the case with a sharp CMB (Fig. 9 in Part 1), making our method of deriving H_{VDSS} and V_p^{av} from T_{VDSS} less accurate. However, the very good agreement between H_{VDSS} and $H_{H\kappa}$ (Fig. 10c) for the SW Slave Craton not only demonstrates the robustness of our method, but also verifies the underlying assumptions that we make about the study area. First, the study area is well approximated with a 1-D lithospheric model. Secondly, the CMB beneath the study area is

sufficiently sharp that *SsPmp* reflections and *Ps* conversions happen at essentially the same depth.

5 CONCLUSIONS

We have shown with synthetic and field examples that T_{VDSS} and Φ_{VDSS} can be used to derive average crustal V_p, crustal thickness and V_p of the uppermost mantle. We have also demonstrated that average crustal V_p/V_s ratio and composition can be estimated with PRF-VDSS joint analysis. Our field example from the SW Slave Craton shows an intermediate crustal composition, together with crustal thickness suggestive of a Mesoarchean formation age.

ACKNOWLEDGEMENTS

We thank Brad Hacker from University of California, Santa Barbara, who provided his compilation of laboratory measurements. We thank the Data Management Center of the Incorporated Research Institutions for Seismology (IRIS-DMC) for the waveforms of the Yellowknife array and Canadian Hazards Information Service for the data of the POLARIS array. We also thank Jieyuan Ning from Peking University and two anonymous reviewers for their valuable advice. Tianze Liu is supported by a Stanford Graduate Fellowship. Gabriel Ferragut was supported by an IRIS internship during his stay at Stanford.

REFERENCES

Aki, K. & Richards, P.G., 2002a. Phase shifts: phase delay and phase advance, in *Quantitative Seismology,* 2nd edn, p. 151, ed. Ellis, J., University Science Books.

Aki, K. & Richards, P.G., 2002b. Reflection and transmission of P-SV across a solid-solid interface, in *Quantitative Seismology,* 2nd edn, pp. 139–145, ed. Ellis, J., University Science Books.

Barruol, G. & Kern, H., 1996. Seismic anisotropy and shear-wave splitting in lower-crustal and upper-mantle rocks from the Ivrea Zone—experimental and calculated data, *Phys. Earth planet. Inter.,* **95,** 175–194.

Bennett, V., Jackson, V.A., Rivers, T., Relf, C., Horan, P. & Tubrett, M., 2005. Geology and U-Pb geochronology of the Neoarchean Snare River terrane: tracking evolving tectonic regimes and crustal growth mechanisms, *Can. J. Earth Sci.,* **42,** 895–934.

Bleeker, W., 2002. Archaean tectonics: a review, with illustrations from the Slave craton, *Geol. Soc. Lond., Spec. Publ.,* **199,** 151–181.

Bostock, M.G., 1998. Mantle stratigraphy and evolution of the Slave province, *J. geophys. Res.,* **103,** 21 183–21 200.

Bowring, S.A. & Williams, I.S., 1999. Priscoan (4.00–4.03 Ga) orthogneisses from northwestern Canada, *Contrib. to Mineral. Petrol.,* **134,** 3–16.

Christensen, N.I., 1996. Poisson's ratio and crustal seismology, *J. geophys. Res.,* **101,** 3139–3156.

Christensen, N.I. & Mooney, W.D., 1995. Seismic velocity structure and composition of the continental crust: a global view, *J. geophys. Res. Solid Earth,* **100,** 9761–9788.

Fernández-Viejo, G. & Clowes, R.M., 2003. Lithospheric structure beneath the Archaean Slave Province and Proterozoic Wopmay orogen, northwestern Canada, from a LITHOPROBE refraction/wide-angle reflection survey, *Geophys. J. Int.,* **153,** 1–19.

Fernández-Viejo, G., Clowes, R.M. & Welford, J.K., 2005. Constraints on the composition of the crust and uppermost mantle in northwestern Canada: *Vp*/*Vs* variations along Lithoprobe's SNorCLE transect, *Can. J. Earth Sci.,* **42,** 1205–1222.

Hacker, B.R., Kelemen, P.B. & Behn, M.D., 2015. Continental Lower Crust, *Annu. Rev. Earth planet. Sci.,* **43,** 167–205.

Hammer, P.T.C., Clowes, R.M., Cook, F.A., van der Velden, A.J. & Vasudevan, K., 2010. The Lithoprobe trans-continental lithospheric cross sections: imaging the internal structure of the North American continent, *Can. J. Earth Sci.,* **47,** 821–857.

Herrmann, R.B., 2013. Computer programs in seismology: an evolving tool for instruction and research, *Seismol. Res. Lett.,* **84,** 1081–1088.

Kang, D., Yu, C., Ning, J. & Chen, W., 2016. Simultaneous determination of crustal thickness and *P* wavespeed by Virtual Deep Seismic Sounding (VDSS), *Seismol. Res. Lett.,* **87,** 1104–1111.

Karplus, M.S. *et al.*, 2019. Receiver-function imaging of the lithosphere at the Kunlun-Qaidam boundary, Northeast Tibet, *Tectonophysics,* **759,** 30–43.

Liu, T., Klemperer, S.L., Yu, C. & Ning, J., 2018. Post-critical SsPmp and its applications to Virtual Deep Seismic Sounding (VDSS)—1: sensitivity to lithospheric 1-D and 2-D structure, *Geophys. J. Int.,* **215,** 880–894.

Luo, S., Zhu, L., Huang, R., Luo, Y., Jiang, X. & Hua, Y., 2018. Determination of crustal thickness and velocities by using receiver functions and PmP travel times, *Geophys. J. Int.,* **216,** 1304–1312.

Parker, E.H., Hawman, R.B., Fischer, K.M. & Wagner, L.S., 2016. Estimating crustal thickness using SsPmp in regions covered by low-velocity sediments: imaging the moho beneath the Southeastern Suture of the Appalachian Margin Experiment (SESAME) array, SE Atlantic Coastal Plain, *Geophys. Res. Lett.,* **43,** 9627–9635.

Porritt, R.W. & Miller, M.S., 2018. Updates to FuncLab, a Matlab based GUI for handling receiver functions, *Comput. Geosci.,* **111,** 260–271.

Randall, G.E., 1989. Efficient calculation of differential seismograms for lithospheric receiver functions, *Geophys. J. Int.,* **99,** 469–481.

Snyder, D. & Bruneton, M., 2007. Seismic anisotropy of the Slave craton, NW Canada, from joint interpretation of SKS and Rayleigh waves, *Geophys. J. Int.,* **169,** 170–188.

Thompson, D.A., Rawlinson, N. & Tkalčić, H., 2019. Testing the limits of virtual deep seismic sounding via new crustal thickness estimates of the Australian continent, **218**(2), *Geophys. J. Int.,* 787–800.

Tian, X. *et al.*, 2015. Weakly coupled lithospheric extension in southern Tibet, *Earth planet. Sci. Lett.,* **430,** 171–177.

Tseng, T.L., Chen, W.P. & Nowack, R.L., 2009. Northward thinning of Tibetan crust revealed by virtual seismic profiles, *Geophys. Res. Lett.,* **36,** 1–5.

van der Velden, A.J. & Cook, F.A., 2002. Products of 2.65–2.58 Ga orogenesis in the Slave Province correlated with Slave-Northern Cordillera Lithospheric Evolution (SNORCLE) seismic reflection patterns, *Can. J. Earth Sci.,* **39,** 1189–1200.

Yu, C., Chen, W.P. & van der Hilst, R.D., 2016. Constraints on residual topography and crustal properties in the western United States from virtual deep seismic sounding, *J. geophys. Res.: Solid Earth,* **121,** 5917–5930.

Yu, C.Q., Chen, W.P., Ning, J.Y., Tao, K., Tseng, T.L., Fang, X.D., John Chen, Y. & van der Hilst, R.D., 2012. Thick crust beneath the Ordos plateau: implications for instability of the North China craton, *Earth planet. Sci. Lett.,* **357–358,** 366–375.

Yu, C.Q., Chen, W.P. & Van Der Hilst, R.D., 2013. Removing source-side scattering for virtual deep seismic sounding (VDSS), *Geophys. J. Int.,* **195,** 1932–1941.

Yuan, H., 2015. Secular change in Archaean crust formation recorded in Western Australia, *Nat. Geosci.,* **8,** 808–813.

Zhu, L. & Kanamori, H., 2000. Moho depth variation in southern California from teleseismic receiver functions, *J. geophys. Res.,* **105,** 2969–2980.

SUPPORTING INFORMATION

Supplementary data are available at *GJI* online.

Text S1. Estimating uncertainties of Φ_{VDSS} and T_{VDSS}.
Table S1. Information of Grade A and B events recorded at YKW3.
Figure S1. Constraining Moho depth and V_p^{um} using synthetic data with 10 per cent white noise.

Figure S2. Distribution of V_p^{um} derived from random simulations of noisy synthetic *SsPmp* waveforms.
Figure S3. Uncertainty estimation for Φ_{VDSS}.
Figure S4. Constraining Moho depth, V_p^{av} and V_p^{um} using synthetic data with 10 per cent white noise.
Figure S5. PRF observations for EDZN.
Figure S6. Effects of data selection on estimated Moho depth, $V_p^{\text{av}}$and V_p^{um}, for real data.

Please note: Oxford University Press is not responsible for the content or functionality of any supporting materials supplied by the authors. Any queries (other than missing material) should be directed to the corresponding author for the paper.